RESEARCH OF PARTICLE STREAK VELOCIMETRY BASED ON LIGHT FIELD ZEMAX SIMULATION

MIAO YANG [1,2]

[1] School of Energy and Power Engineering, University of Shanghai for Science and Technology, Shanghai 200093, China
[2] Shanghai Key Laboratory of Multiphase Flow and Heat Transfer in Power Engineering, Shanghai 200093, China

Abstract. Light field imaging technology can capture the light intensity and particle propagation direction within a single exposure, thereby achieving three-dimensional imaging while simplifying experimental complexity. Compared to conventional methods such as particle image velocimetry and particle tracking velocimetry, particle streak velocimetry (PSV) extends the upper limit of measurable velocity, operates effectively under lower light intensities, and offers pronounced advantages in high-speed flow field analysis. The integration of light field imaging and PSV measurement techniques combine the strengths of both methods, making this approach particularly promising for three-dimensional flow field investigations. Despite its potential, this area remains underexplored. Previously, the author has developed a three-dimensional flow field experimental measurement system based on light field PSV. In this article, the author employs Zemax software to construct a Galileo-type simulated light field imaging system in non-sequential mode. The imaging characteristics of this system were analyzed, yielding a depth calibration curve for the simulated virtual light field imaging system and a synthetic three-dimensional trajectory map. The algorithm reconstructed the three-dimensional trajectory by integrating the depth calibration curve with a light field PSV-based three-dimensional flow field measurement and processing algorithm. This study establishes a Zemax simulation framework for light field PSV, offering critical simulation data to advance research in three-dimensional flow field measurement utilizing light field PSV.

1. Introduction

The three-dimensional reconstruction of fluid flows is essential in many areas, including industry, agriculture, medicine, environmental science, and aerospace. The conventional methods for 3D flow field reconstruction often involve complex setups with multiple cameras and intricate optical paths, which makes them less practical. The light field imaging method simplifies these issues by capturing the light intensity and the propagation direction with a single shot. This technology simplifies experimental setups in the presence of constraints. It enables the rapid acquisition of large volumes of 3D data, making it ideal for studying complex flow phenomena that demand extensive data collection.

The pioneering work of A. Gershun [1] and the all-optical function model laid the foundation for light field imaging. However, computing this function is challenging due to the large number of parameters. In 1995, L. McMillan and G. Bishop [2] simplified this model from seven to five dimensions, and a year later, M. Levoy and P. Hanrahan [3] further reduced it to four dimensions by parameterizing the light rays using two parallel planes. These breakthroughs paved the way for advancements in light field imaging.

After 2000, the field expanded into an interdisciplinary topic. Improvements in optical design, such as microlens arrays, enhanced the ability of light field cameras to capture detailed information about the target. New algorithms in digital image processing further improved the efficiency of handling light field data. For example, in 2002, J. Yang et al. [4] created an array of 64 cameras and developed a distributed rendering algorithm to manage the data bandwidth problem caused by the large number of cameras in traditional dynamic light field systems.

By 2005, progress in camera design and algorithm optimization allowed portable light field cameras to become a reality, thanks to innovations by B. Wilburn et al. [5]. The same year, R. Ng et al. [6] at Stanford University developed the first handheld light field camera. This device allowed users to refocus images after capturing them, a revolutionary feature demonstrating the potential of the technology. They also demonstrated how post-processing could replicate the depth-of-field effects of a small aperture while maintaining the advantages of shooting with a large aperture.

In 2006, D. Lanman et al. [7] designed a spherical reflective array imaging system, and by conducting a geometric analysis and calibration of the system, they derived a relationship between mapped pixel coordinates and three-dimensional spatial rays. In 2007, A. Veeraraghavan et al. [8] proposed using attenuation masks in conventional cameras to modulate the light field, achieving high spatial resolution but at the cost of light loss. By 2010, Y. Taguchi et al. [9] introduced a method to capture light field data by moving a camera along a mirror rotation axis, significantly enhancing the capabilities of light field cameras.

The release of Lytro's first consumer light field camera in 2011 marked a turning point. In 2013, innovations by K. Venkataraman et al. [10] and C. Kim et al. [11], namely algorithms for high-resolution light field data processing, pushed the boundaries even further. These advancements made light field imaging more accessible and practical for various applications, from virtual reality to everyday photography.

During the same year, K. Marwah et al. [12] proposed a novel compressed light field camera architecture that can restore higher resolution light fields from a single image. X. Lin's team [13] 2015 proposed a camera array-based light field microscope that overcame traditional resolution limitations but struggled with angular resolution for samples with large depth ranges or slender structures. Their system's larger volume also made integration into microdevices challenging.

In 2016, N. Antipa et al. [14] introduced a method to capture 4D light field data using a single 2D sensor image, avoiding light loss issues and ensuring higher luminous flux, lower costs, and greater flexibility. However, the system's computational requirements were significant, and angular resolution limitations remained unresolved.

By 2019, Z.P. Tan and colleagues [15] developed a modular light field adapter for high-speed cameras, enabling time-resolved 3D flow measurement with a single camera. This adapter marked a shift in light field imaging applications, expanding into areas like autonomous driving, robotics, 3D modeling, and medical imaging. Recently, researchers have focused on processing large-scale light field data in real-time, leveraging technologies like quantum computing and AI to push the boundaries further.

In recent years, much research on light field imaging systems combined with other flow field measurement methods has emerged such as: In 2020, X. Zhu et al. reconstructed the three-

dimensional velocity field based on a single light field camera combined with PIV velocity measurement technology [16]. In the same year, A.Z. Kvon et al. used the light field particle tracking velocimetry (PTV) technology combined with the fluorescence tracer technology. They proved that the light field PTV technology could be used for the three-dimensional wave measurement of liquids with different physical properties [17]. The research of the light field combined with PSV is less. Yet, PSV offers unique advantages: it can measure higher motion speeds, operate under lower light intensities, and function with continuous light sources, eliminating the need for expensive pulsed lasers. PSV also simplifies system complexity and reduces costs, as it typically requires only a single camera for 3D measurements. Unlike PTV, which can suffer from particle matching errors, PSV analyzes stripe images for continuity and direction, reducing such errors [18]. In 2023, X. Dong et al. [19] proposed a PSV three-dimensional velocity measurement method based on defocus by analyzing the gray value distribution of particle trajectory images. The speed measurement method combining PSV with other methods has also appeared. S. Sold et al. extended the measuring range of PSV through PTV. However, this method is only used for two-dimensional velocity field measurements [20]. Combining light field imaging with PSV harnesses the strengths of both technologies.
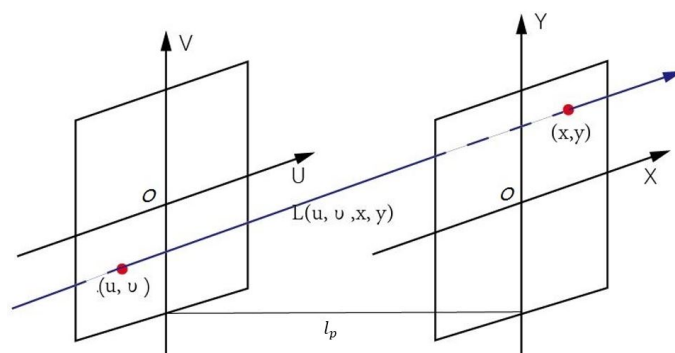
In 2024, the author [21] introduced a 3D flow field velocity measurement method based on light field PSV and demonstrated its feasibility through experiments. This study constructs a Galileo-type light field imaging system using Zemax software, analyzes its imaging characteristics, and develops algorithms to derive depth calibration curves. The algorithms simulated 3D trajectory images of pixel block motion and integrated these with the depth calibration curve and PSV algorithm, retrieving precise information about the 3D motion.

2. Principles of light field PSV measurement
2.1. Parameterized representation of light field imaging
The theoretical background of light field imaging is the all-optical function, [22] an optical concept that assigns radiance values to light rays propagating in physical space and describes its distribution in space. The all-optical function is expressed as $I_\lambda(x, y, z, \theta, \Phi, \lambda, t)$, where I_λ represents the spectral radiance per unit time, (x, y, z) is the spatial position point coordinate, (θ, Φ) is the incident direction, λ is the wavelength of light, and t is the time point.

By introducing additional constraints, the all-optical function reduces to four dimensions: i) the dependence of the all-optical function on the time dimension is removed by integrating over the exposure time; ii) the light field is usually considered monochromatic, and the spectral dimension of the all-optical function is eliminated by integrating the spectral sensitivity of camera pixels; iii) assuming that light propagates in a vacuum without any medium or obstruction, the direction of light propagation remains unchanged, which removes another dimension from the all-optical function [3].

Fig. 1. Diagram illustrating the parameterized representation of a four-dimensional light field.

Therefore, the light field can be parameterized using two parallel planes and a ray passing through the parallel planes, as shown in Fig. 1.

In the Fig. 1, the *UOV* and the *XOY* planes are parallel. *L* is a ray that passes through the *UOV* and *XOY* plane, with radiation energy denoted as *L* (u, v, x, y). The intersection points of ray *L* with the two planes are (u, v) and (x, y), respectively. The distance between the two parallel planes is l_p, and the total energy received at point (x, y) from beam *L* can be expressed as:

$$I(u,v) = \iint L(u,v,x,y)\,\mathrm{d}u\,\mathrm{d}v. \tag{1}$$

2.2. Parameterized representation of ray tracing in optical field systems

Fig. 2 shows the optical field parameterized with parallel planes UO_1V and XO_2Y, where L_m represents a ray propagating in a spatially uniform medium. The intersection point of the main optical axis *Z* with plane UO_1V is O_1, and the intersection point with plane XO_2Y is O_2. The main optical axis, *Z*, is perpendicular to both planes.
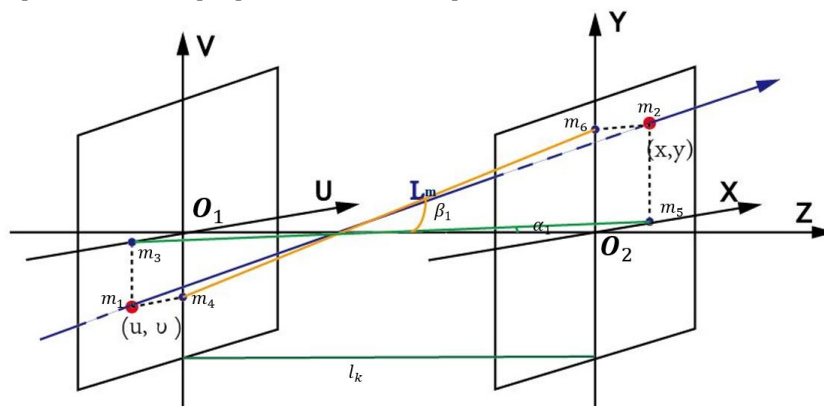

Fig. 2. Diagram illustrating the characterization of ray propagation.

The intersection point of ray L_m with plane UO_1V is denoted as $m_1(u_1,v_1,\alpha_1,\beta_1)$, and the intersection point with plane XO_2Y is denoted as $m_2(x_1,y_1,\alpha_1,\beta_1)$, where (u_1,v_1) is the coordinate of point m_1 on plane UO_1V, and (x_1,y_1) is the coordinate of point m_2 on plane XO_2Y. Point m_3 is the projection of m_1 onto the *U* axis; point m_4 is the projection of m_1 onto the *V* axis; point m_5 is the projection of m_2 onto the *X* axis, and point m_6 is the projection of m_2 onto the *Y* axis.

Here, α_1 represents the directional coordinate of ray L_m along the *U* axis, β_1 represents the directional coordinate of ray L_m along the *V* axis, and the propagation distance from m_1 to m_2 along the *Z* axis (i.e., the distance between the two planes) is denoted as l_k. The coordinate definition of point m_2 follows the same principle.

The ray tracing process of a light field camera involves four steps: (1) the propagation of light rays from the emitting point to the main lens plane; (2) the propagation of light from the main lens plane to the microlens plane; (3) the propagation of light from the microlens plane to the CCD plane; and (4) the conversion of detector coordinates to the pixel coordinate system. According to the linear optical tracing model [3, 23-25], the ray tracing process is shown in Fig. 3, and the tracing formula is as follows:

light propagating from the luminous point to the main lens plane:
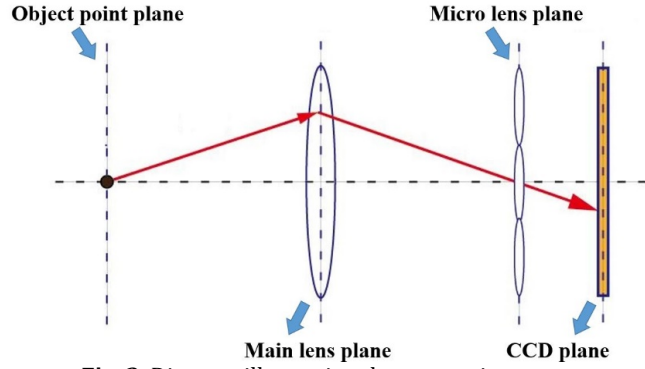
Fig. 3. Diagram illustrating the ray tracing process.

$$\begin{bmatrix} x_1 \\ y_1 \\ \tan\alpha_1' \\ \tan\beta_1' \end{bmatrix} = \begin{bmatrix} 1 & 0 & 0 & l_k \\ 0 & 1 & l_k & 0 \\ 0 & 0 & 1 & 0 \\ 0 & 0 & 0 & 1 \end{bmatrix} \begin{bmatrix} u_1 \\ v_1 \\ \tan\alpha \\ \tan\beta_1 \end{bmatrix}, \tag{2}$$

when the light is near the axis, then $\alpha_1(\alpha_1') \approx tan\alpha_1(tan\alpha_1')$.

propagation of light from the main lens plane to the microlens plane:

$$\begin{bmatrix} x_2 \\ y_2 \\ \tan\alpha_2' \\ \tan\beta_2' \end{bmatrix} = \begin{bmatrix} 1 & 0 & 0 & 0 \\ 0 & 1 & 0 & 0 \\ -1/f_L & 0 & 1 & 0 \\ 0 & -1/f_L & 0 & 1 \end{bmatrix} \begin{bmatrix} u_2 \\ v_2 \\ \tan\alpha_2 \\ \tan\beta_2 \end{bmatrix}. \tag{3}$$

Here, f_L presents the focal length of the main lens, and the light coordinates passing through the main lens are $(u_2,\upsilon_2,\alpha_2,\beta_2)$. The coordinates of the light after passing through the main lens are $(x_2,y_2,\alpha_2',\beta_2')$. When the light is near the optical axis, $\alpha_2(\alpha_2') \approx tan\alpha_2(tan\alpha_2')$. Light propagation from the microlens plane to the sensor plane:

$$\begin{bmatrix} x_3 \\ y_3 \\ \tan\alpha_3' \\ \tan\beta_3' \end{bmatrix} = \begin{bmatrix} 1 & 0 & 0 & 0 \\ 0 & 1 & 0 & 0 \\ -1/f_m & 0 & 1 & 0 \\ 0 & -1/f_m & 0 & 1 \end{bmatrix} \begin{bmatrix} u_3 \\ v_3 \\ \tan\alpha_3 \\ \tan\beta_3 \end{bmatrix} + \begin{bmatrix} 0 \\ 0 \\ k_x/f_m \\ k_y/f_m \end{bmatrix}. \tag{4}$$

Here, f_m denotes the focal length of the microlens, and the coordinates of the ray before passing through the microlens are $(u_3,v_3,\alpha_3,\beta_3)$. The coordinates of the ray after passing through the microlens are $(x_3,y_3,\alpha_3',\beta_3')$, where (k_x, k_y) represents the coordinate of the center of a single microlens on the XO_2Y plane. When the light is near the optical axis, $\alpha_3(\alpha_3') \approx tan\alpha_3(tan\alpha_3')$.

Mapping detector coordinates to the pixel coordinate system:

$$\begin{bmatrix} u_p \\ v_p \\ 1 \end{bmatrix} = \begin{bmatrix} round\left(\dfrac{u_4}{P_x}\right) & 0 & 1 \\ round\left(\dfrac{v_4}{P_y}\right) & 1 & 0 \\ 1 & 0 & 0 \end{bmatrix} \begin{bmatrix} 1 \\ \dfrac{n_x+1}{2} \\ \dfrac{n_y+1}{2} \end{bmatrix}. \tag{5}$$

Here, (P_x, P_y) the value of a single pixel block on the sensor, (n_x, n_y) denotes the number of pixels on the sensor in the X and Y directions, and (u_4, v_4) is the coordinate of the intersection point between the light ray and the detector plane on the world coordinate system *XOY*. Similarly, (u_p, v_p) represents the coordinate of the light ray in the pixel coordinate system *UOV.* Tracking as much light as possible can improve imaging clarity, but tracking efficiency must also be considered [26].

2.3. Principles of imaging in a light field camera

Light field cameras can be categorized into focusing and non-focusing types. Focusing light field cameras are further classified into Galilean and Kepler types based on the distance between the microlens array and the CCD.

A non-focusing optical field camera, also known as an all-optical camera, establishes a conjugate relationship between the object point plane and the microlens array plane relative to the main lens plane. The distance from the microlens array plane to the CCD plane is twice the focal length of the microlens. The imaging principle of a non-focused light field camera is illustrated in Fig. 4.
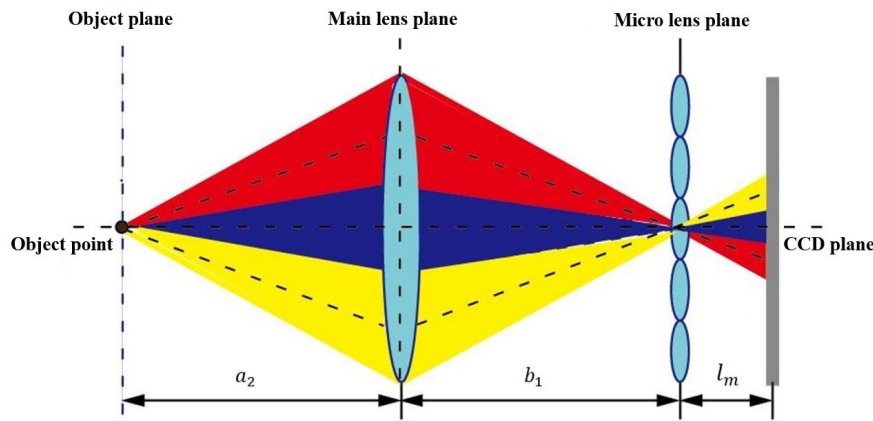

Fig. 4. Imaging principle of a non-focusing light field camera.

As shown in Fig. 4, the distance from the object point plane to the main lens is denoted as α_2 the distance from the main lens plane to its imaging plane is denoted as b_1, and the distance from the microlens plane to the CCD plane is denoted as l_m. The focal length of the main lens is represented by f_L, and the focal length of the microlens is represented by f_m. According to the Gaussian imaging formula, the following relationship holds:

$$\begin{cases} \dfrac{1}{a_2} + \dfrac{1}{b_1} = \dfrac{1}{f_L} \\ \dfrac{1}{b_1} + \dfrac{1}{l_m} = \dfrac{1}{f_m} \end{cases} \tag{6}$$

Focused light field cameras are categorized into Kepler-type and Galileo-type light field cameras. Unlike non-focusing light field cameras, the microlens array in focusing light field cameras is not positioned at a distance equal to the focal length of a single microlens from the CCD plane.

(1) Kepler-type light field camera.

Fig. 5 illustrates a schematic diagram of the imaging principle of the Kepler-type light field camera. In this scheme, d represents the distance from the object point plane to the front face of the main lens, while a_1 is the distance from the front face of the main lens to the
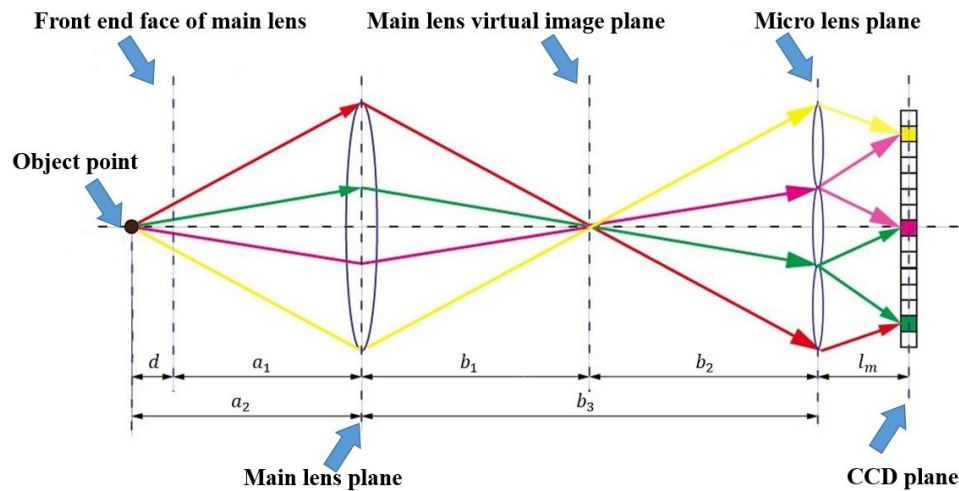
Fig. 5. Imaging principle of a Kepler-type light field camera.

plane. The distance from the object point plane to the main lens plane is denoted as a_2. The distance from the main lens plane to the virtual image plane of the main lens is represented by b_1. The distance from the virtual image plane of the main lens to the plane of the microlens is represented by b_2. The distance from the main lens plane to the microlens plane is represented by b_3, and l_m denotes the distance from the microlens plane to the CCD plane. The focal lengths of the main lens and microlens are represented by f_L and f_m, respectively. According to the Gaussian imaging formula, the following relationships apply:

$$\begin{cases} \dfrac{1}{a_2} + \dfrac{1}{b_1} = \dfrac{1}{f_L} \\ \dfrac{1}{l_m} + \dfrac{1}{b_2} = \dfrac{1}{f_m} \end{cases}. \tag{7}$$

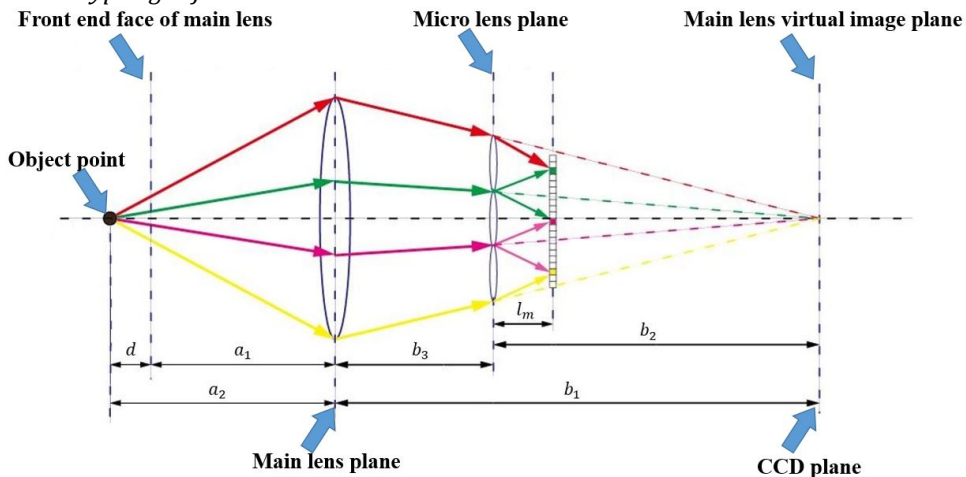*(2) Galileo-type light field camera.*

Fig. 6. Imaging principle of a Galileo-type light field camera.

Fig. 6 presents a schematic diagram of the imaging principle of the Galileo-type light field camera. The symbols have the same meanings as those used for Kepler-type light field cameras. According to the Gaussian imaging formula, the following relationships hold:

$$\begin{cases} \dfrac{1}{a_2} + \dfrac{1}{b_1} = \dfrac{1}{f_L} \\ \dfrac{1}{l_m} - \dfrac{1}{b_2} = \dfrac{1}{f_m} \end{cases}. \tag{8}$$

The distance from the microlens array surface of the Kepler-type light field camera to the CCD plane $f_m < l_m < \dfrac{3}{2} f_m$. Similarly, the distance from the microlens array surface of the Galileo-type light field camera to the CCD plane satisfies $\dfrac{1}{2} f_m < l_m < f_m$.

2.4. Principles of light field rendering

The microlens array in a non-focusing light field camera is placed directly on the imaging surface of the main lens. This array separates the light that passes through the main lens at different angles, projecting it onto the CCD sensor. Fig. 7 illustrates the rendering principle of this type of camera. Each microlens re-creates an image formed by the main lens. The total number of microlenses determines the spatial sampling rate of the camera, while the number of pixels beneath each microlens sets the angular sampling rate.

Pixels are extracted from the same position within each sub-image to generate a single-view image from a non-focused light field camera. These pixels are then stitched together based on their positions in the corresponding sub-images. This process provides access to a wealth of angular information but comes with a trade-off: the spatial resolution of the final image is reduced.
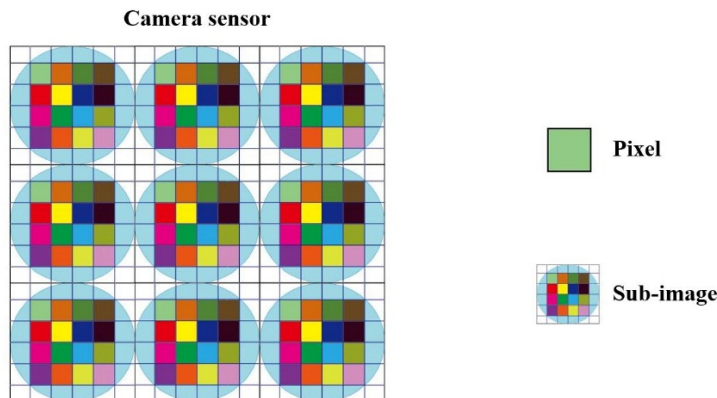

Fig. 7. Diagram of the rendering principle of a non-focusing light field camera.

When obtaining each angle information, the focused light field camera extracts does not extract individual pixels at the same position in the sub-image but instead extracts an entire pixel block composed of $P_x \times P_y$ pixels. Suppose the captured light field image contains $N_x \times N_y$ sub-images, each with $E_x \times E_y$ pixels. Finally, the pixel blocks at the same position, extracted from each sub-image, are reassembled according to the sub-image positions to generate the image corresponding to a specific viewing angle. By using a focused light field camera, the redundancy of angular resolution is traded for increased spatial resolution, thereby improving the overall image quality.

2.5. Refocusing and depth measurement principles

Light field images contain information about light rays within a spatial volume, and refocusing involves extracting the four-dimensional information of light rays from the light

field image and focusing them onto a specific plane. The schematic diagram of the refocusing principle is shown in Fig. 8.
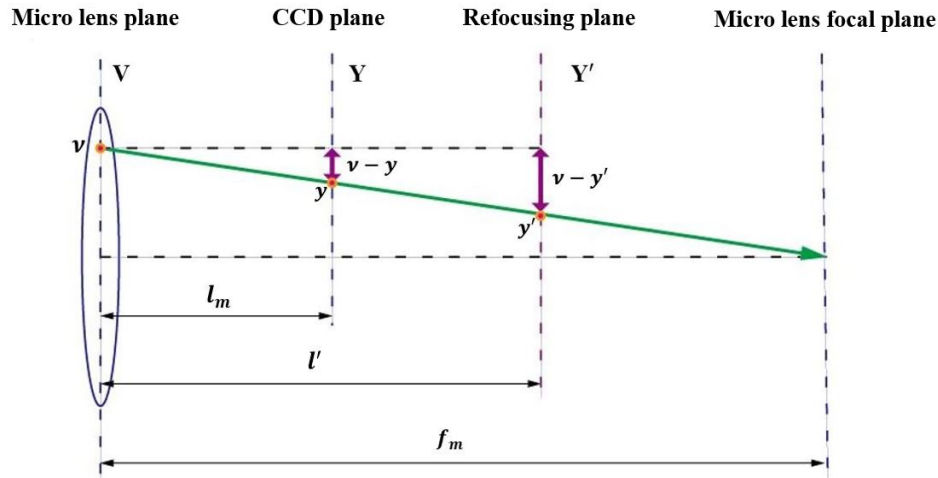
Fig. 8. Schematic diagram of the refocusing principle.

Here, V represents the microlens plane, Y represents the CCD plane, and Y' represents the refocusing plane, l_m denotes the distance from the microlens plane to the CCD plane, l' represents the distance from the microlens plane to the refocusing plane, and f_m is the focal length of the microlens. The intersection points of light passing through the microlens, CCD, and refocusing planes are v, y, y', respectively. According to the principle of similar triangles, the following relationships hold:

$$\frac{l_m}{l'} = \frac{v - y}{v - y'}.$$ (9)

If $\dfrac{l'}{l_m} = \alpha$, then:

$$y = \frac{1}{\alpha}y' + \left(1 - \frac{1}{\alpha}v\right).$$ (10)

Similarly, in the other two dimensions the following relationship holds:

$$x = \frac{1}{\alpha}x' + \left(1 - \frac{1}{\alpha}u\right).$$ (11)

Substituting Eqs. (10) and (11) into Eq. (1) yields:

$$I(x',y') = \iint L\left(u,v,\frac{1}{\alpha}x' + \left(1 - \frac{1}{\alpha}u\right), \frac{1}{\alpha}y' + \left(1 - \frac{1}{\alpha}v\right)\right) \mathrm{d}u \mathrm{d}v.$$ (12)

Changing α adjusts the position of the refocusing plane, and the refocused image obtained at a specific α corresponds to the image information captured from a particular perspective. When the object under test is most clearly imaged on a specific refocusing plane, the α value at that point is referred to as the optimal refocusing coefficient and is denoted by α_0.

Taking Kepler-type light field camera as an example, Fig. 9 illustrates the following components: ① Object point plane; ② Front end face of the main lens; ③ Main lens plane; ④ Main lens imaging surface; ⑤Microlens array plane; ⑥ CCD plane; ⑦Refocusing plane; ⑧Focal plane of the microlenses. When the light is refocused on plane ⑦ and forms a clear image, the following relationships hold:
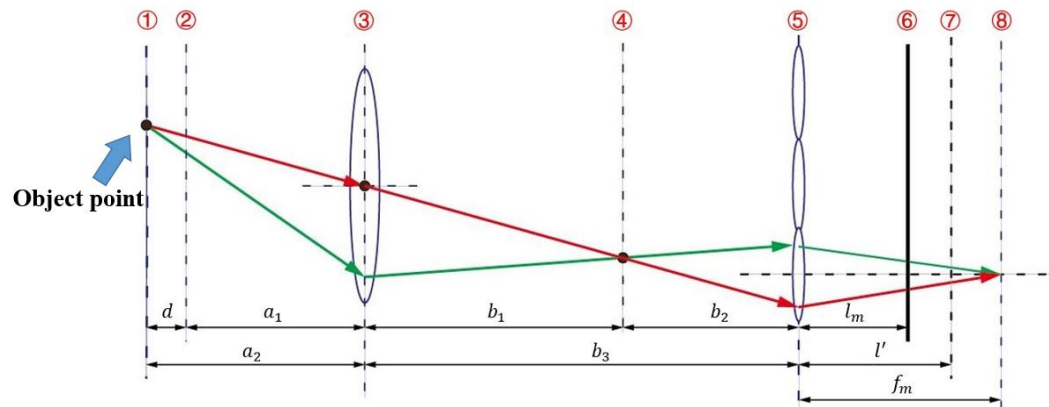
Fig. 9. Schematic diagram of depth measurement principle.

$$\begin{cases} \dfrac{1}{a_2} + \dfrac{1}{b_1} = \dfrac{1}{f_L} \\ \dfrac{1}{l_m\alpha_0} + \dfrac{1}{b_2} = \dfrac{1}{f_m} \end{cases}. \tag{13}$$

Here, $a_2 = a_1 + d$, $b_3 = b_1 + b_2$, $l' = l_m\alpha_0$. Simplify Eq. (13) to yield:

$$d = \left\{ f_L^{-1} - \left[b_3 - \left(f_m^{-1} - (l_m\alpha_0)^{-1} \right)^{-1} \right]^{-1} \right\}^{-1} - a_1. \tag{14}$$

Therefore, for a determined depth position, a one-to-one correspondence exists between d and α_0.

2.6. Principle of three-dimensional flow field measurement in a PSV light field

Fig. 10 shows a schematic diagram of the measurement principle of light field PSV. According to the applicable characteristics of PSV, relatively sparse tracer particles are scattered in the flow field to represent the flow characteristics. A controller controls the triggering of the light field camera and the light source simultaneously, capturing the particle trajectory map within the flow field. The particles' three-dimensional velocity field can be obtained by processing the flow field trajectory map.
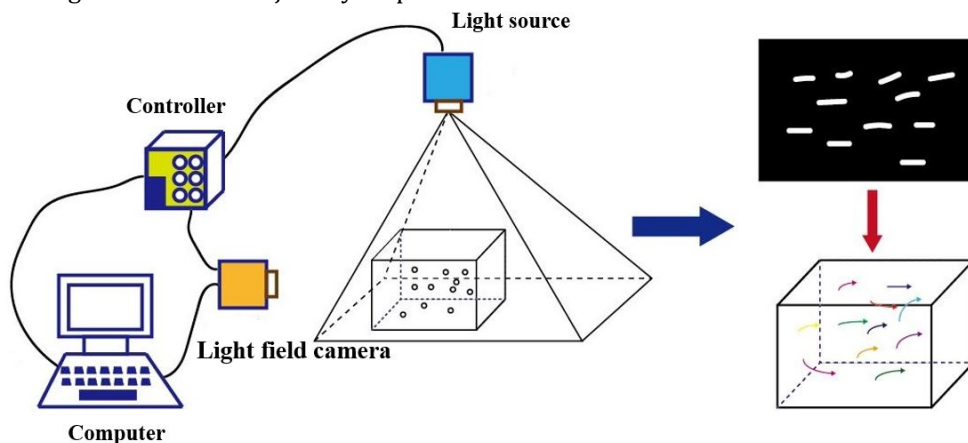

Fig. 10. Schematic diagram of the PSV measurement principle in a light field.

Light field particle image processing involves two main steps: identifying two-dimensional trajectories and confirming three-dimensional depth information. The method requires the following steps: i) depth information acquisition, calibration of the microlens center, and determining key parameters such as magnification and the camera's internal characteristics. These substeps prepare the system for extracting the necessary data. Next, refocusing calibration plates at different positions to create a relationship curve between d (the depth position) and α_0 (the refocusing coefficient). Finally, this data will generate and process the depth map. ii) identifying two-dimensional trajectories, i.e., beginning by applying refocusing and full-focusing processing to the captured flow field images, using preprocessing methods to clean and enhance the images. These substeps include threshold segmentation, dilation, erosion, removing artifacts, skeleton extraction, and eliminating cross lines. The result is a clear two-dimensional trajectory image. iii) calculating three-dimensional trajectories and velocities, i.e., combining the α_0 values of each pixel in the preprocessed focused image with the depth calibration curve and depth map to calculate three-dimensional particle trajectories; determination of the velocity field by dividing the calculated trajectories by the exposure time.

Following this process, a robust algorithm for three-dimensional flow velocity measurement using light field PSV is established.

3. Zemax-simulated light field imaging system construction

Zemax is a professional ray tracing software widely used in optical design, providing both sequential and non-sequential modes. The primary difference between these two modes is that, in non-sequential mode, rays do not interact with objects or surfaces in a predefined order, while in sequential mode, the interaction order of light with surfaces is explicitly defined.

This article establishes a simulated virtual Galileo light field camera model in non-sequential mode. The principle of Galileo's light field camera is the same as that of Kepler's light field camera. The virtual light field camera built here is the Galileo model. Whether a Galileo light field camera or a Kepler light field camera, the relationship between d and α_0 is inversely proportional within a specific imaging range. Fig. 11 shows the color spectrum of incident light in the virtual system. The curve in Fig. 11a is the light source's spectral curve, representing the light source's emission distribution at different wavelengths. Among them, point A represents incandescent lamps with a color temperature of 2856 K. Points B represents sunlight, with a color temperature of 4874 K, C represents daytime light with a color temperature of 6774 K, D represents standard daylight (D65 in the figure, indicating a color temperature of 6500 K), and E represents an ideal light source with no fixed color temperature. In Fig. 11b, "Relative weight" reflects the relative intensity of a specific wavelength of light in the entire spectrum of the light source.

The light field imaging system consists of a main lens, a microlens array, and a CCD. The design of a light field imaging system mainly includes four components: i) design of the main lens, ii) design of the microlens array, iii) selection of the CCD, and iv) adjustment and optimization of ray tracing and distances for each imaging plane.

When designing such systems, special attention should be paid to the conjugate relationship between related surfaces and the matching of F-numbers. The microlens shape is hexagonal in all the simulation systems described in this article. The relationship between

the distance l_m from the microlens array surface of the Galileo light field camera to the CCD imaging surface and the focal length f_m of the microlens is given by $0.5f_m < l_m < f_m$.
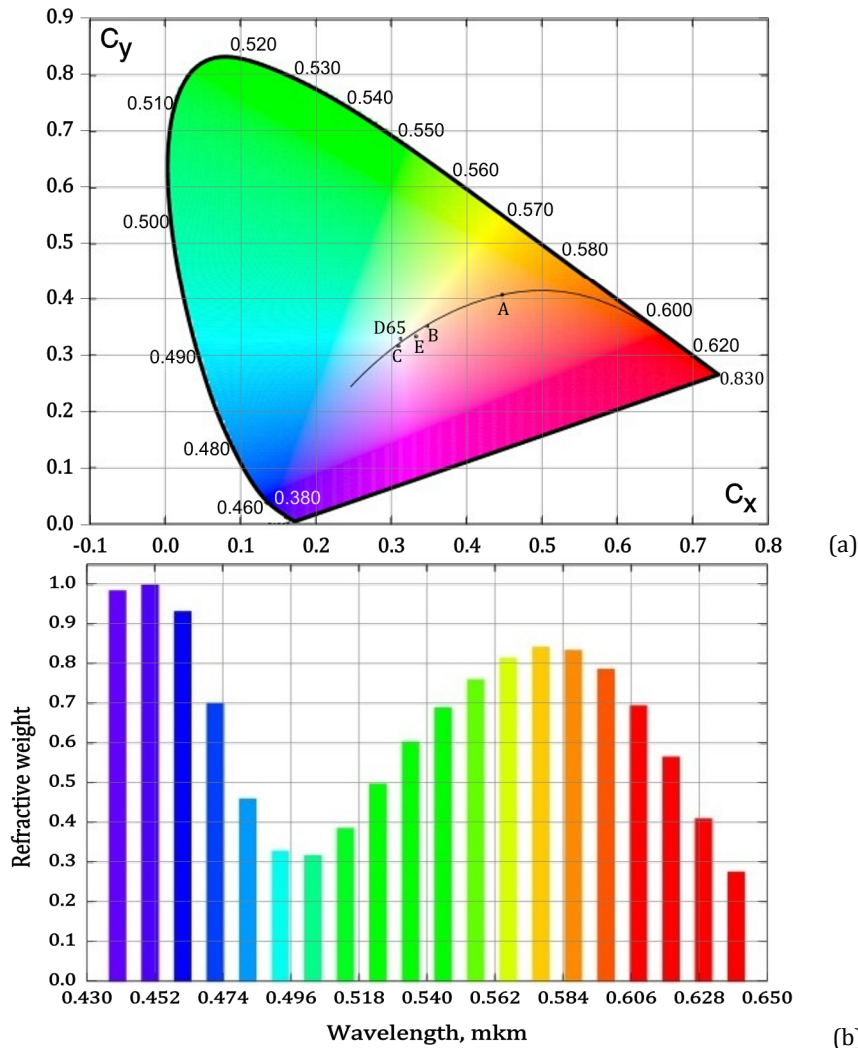

Fig. 11. Color space (a) and dependence of relative weight on the wavelength (b) of incident light in the virtual system.

This article simulates two types of Galileo light field camera imaging systems. The first is the traditional type, where the main lens is composed of a lens group. Fig. 12 shows the shadow mode diagram of the simulated traditional Galileo light field camera imaging system. In Zemax, the shadow mode map is a visualization tool used to display the shadow effects of light as it propagates through an optical system. Through the shadow mode map, users can see the propagation paths of light in the optical system and the shadowed areas it projects onto surfaces or other optical elements. It helps users analyze how light interacts with optical components, ensuring efficient transmission and minimizing unnecessary loss.

The simulations showed that the traditional Galileo light field camera imaging has a very small depth of clear imaging. An ideal lens was added to the original light field camera imaging system to address this issue, significantly improving the imaging depth. Fig. 13 compares simulated optical paths for the two Galileo light field cameras.
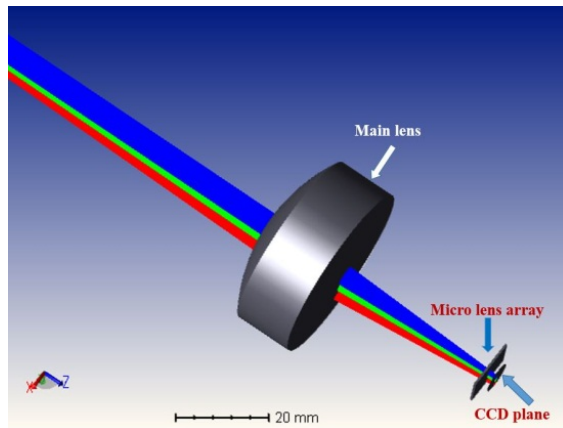
Fig. 12. Shadow mode map of a traditional Galileo light field camera.
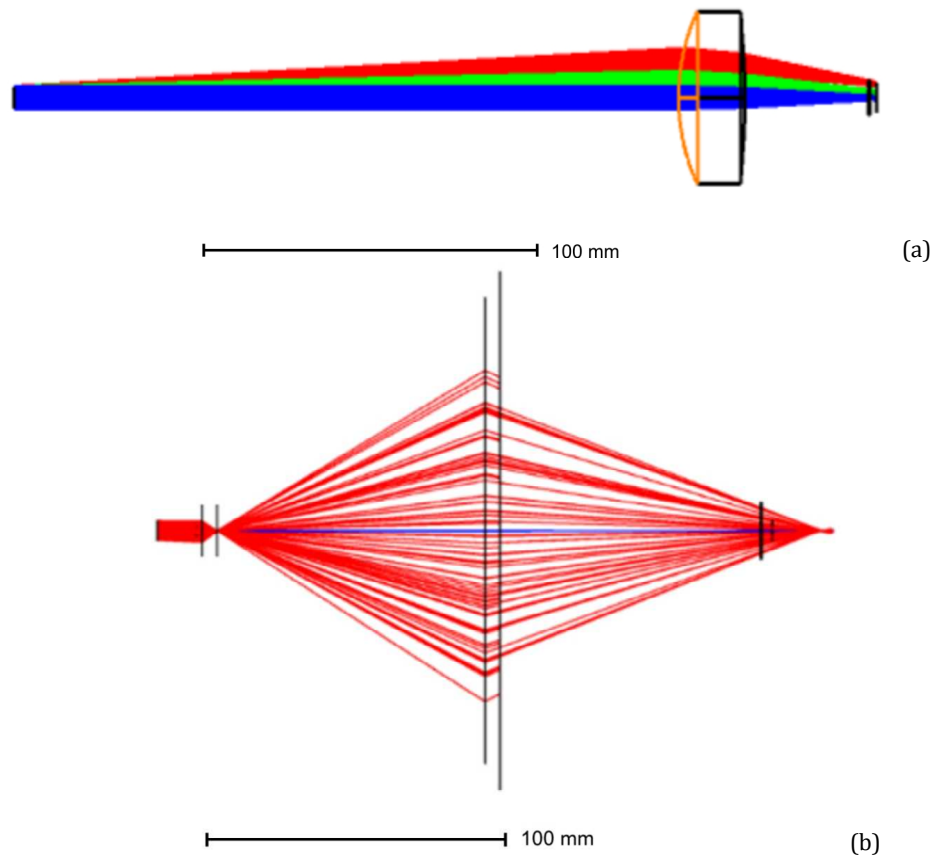
Fig. 13. Comparison of the simulated optical paths for two Galileo light field cameras: (a) light path simulation for a traditional Galileo light field camera; (b) light path simulation for an improved Galileo light field camera.

Table 1 presents the parameters of the improved Galileo light field camera system at a working distance of 5 mm. In this system, the main lens is composed of multiple lens groups, and during the design process, the F-number of the main lens and the microlens are assumed to be equal. The microlens' shape is hexagonal and arranged in a honeycomb pattern.

Fig. 14 shows the angle diagram of the light source in the simulation system, while Fig. 15 displays the shadow pattern diagram of the improved Galileo light field camera imaging system.
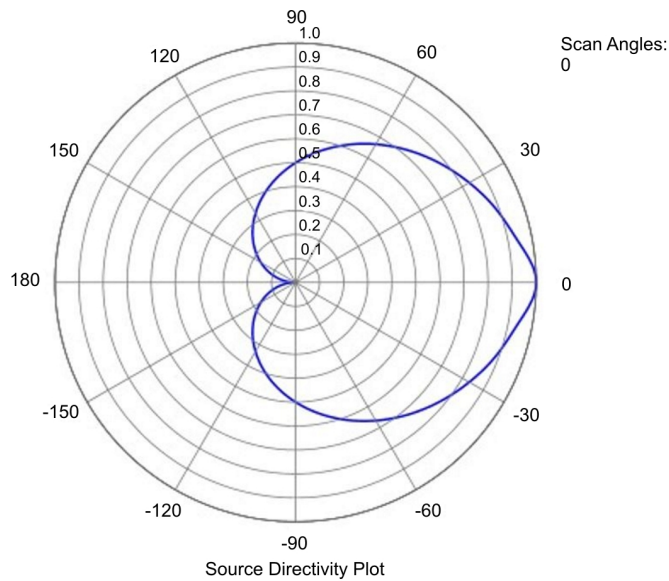
Fig. 14. Angle diagram of the light source in the simulated system.

Table 1. Parameters of the improved Galileo light field camera system

| Parameter	Quantity	unit
Distance from the object surface to the main lens	5	mm
Diaphragm diameter	4	mm
Microlens' focal length	5	mm
Distance from the main lens to the virtual image plane	62.5	mm
Distance from the virtual image plane to the microlens	-20	mm
Distance from the microlens array to the CCD	3.983	mm
Single pixel size	0.0031	mm
Sensor Size	18.7×10.7	mm
Sensor pixel count	6223×3556	pcs
Number of microlenses in the array	147×84	pcs
Number of pixels covered by a single microlens	41	pcs
Single microlens circumdiameter	0.127	mm
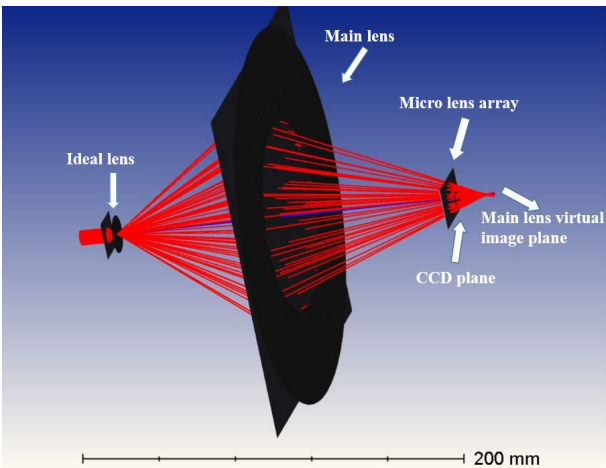
Fig. 15. Fan-shaped diagram of light rays in the improved Galileo light field camera system.

## 4. Calibration and analysis of Zemax-simulated light field imaging system

4.1. Analysis

In the Galileo simulation light field imaging system, a whiteboard was introduced to trace 3×10^8 light rays. The imaging results are compared with those of the commercial Raytrix R12 Micro, as shown in Fig. 16. The comparison shows that the imaging effect is essentially the same as that of commercial light field cameras.

(a)   (b)
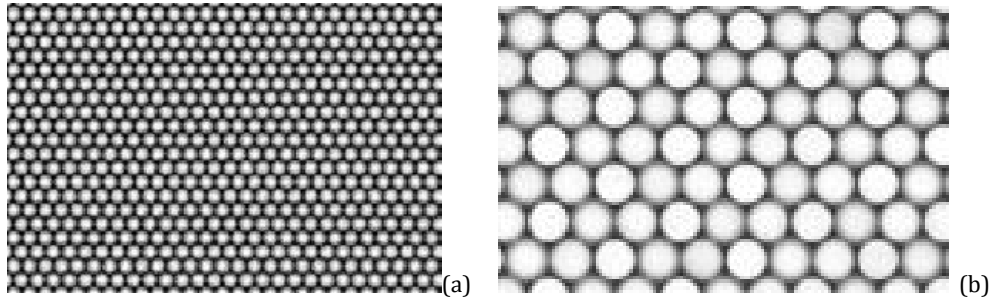
Fig. 16. Comparison of whiteboard imaging using a light field camera: (a) whiteboard image from the simulated light field system; (b) whiteboard image captured by the Raytrix R12 Micro.

By importing the example diagram of the ZEMAX system into the improved Galileo light field system and tracing 3×10^8 rays, the light field imaging comparison diagram was obtained under different working distances (Fig. 17). It can be seen that the imaging effect is consistent with the theory (see Eq. 14).

The simulations show that increasing the number of rays used for tracking results in higher intensity and clearer images. However, this also causes the program to run slower.

(a)   (b)   (c)

(d)   (e)   (f)
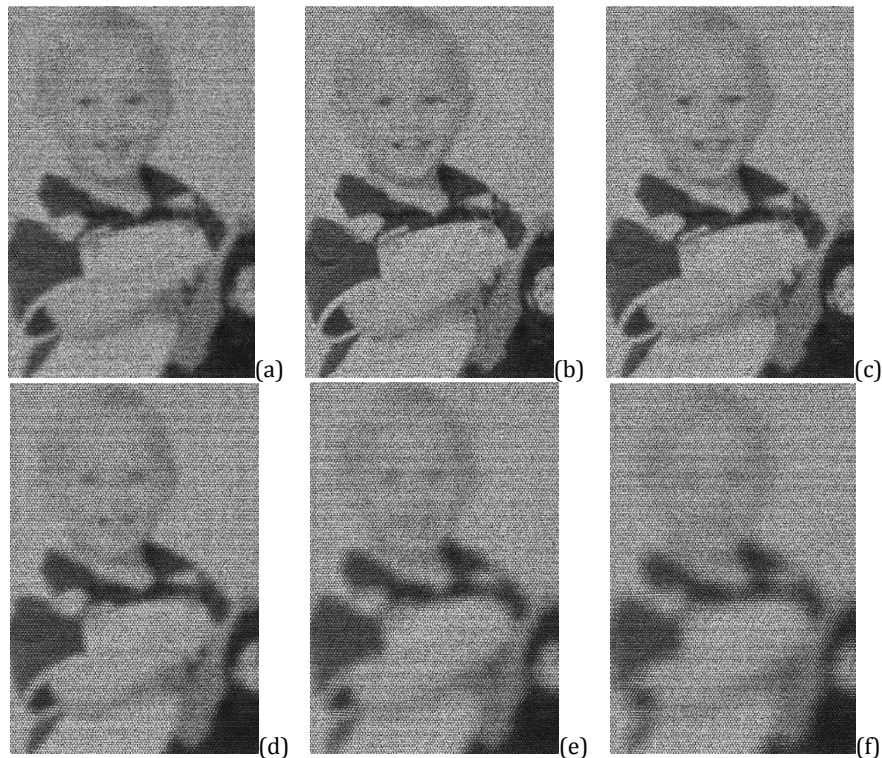
Fig. 17. Imaging comparison of the improved Galileo light field camera at different working distances: (a) d=8mm, (b) d=7mm, (c) d=6mm, (d) d=5mm, (e) d=4mm, (f) d=3mm.
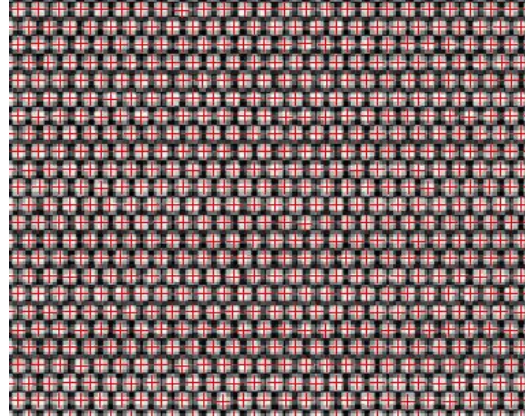
4.2. Calibration

For calibration, it is necessary to import the image of the dot calibration board into the simulated Galileo light field imaging system and trace 3×10^8 light rays. Similarly, it is necessary to adjust the imaging distance by moving from the clearest imaging position d=7 mm to a position closer to the front of the lens in 1 mm increments, recording the imaging results at each step. This process has to be continued until the imaging object is no longer visible. Fig. 18 shows the comparison images of the dot calibration plate obtained at different imaging distances.
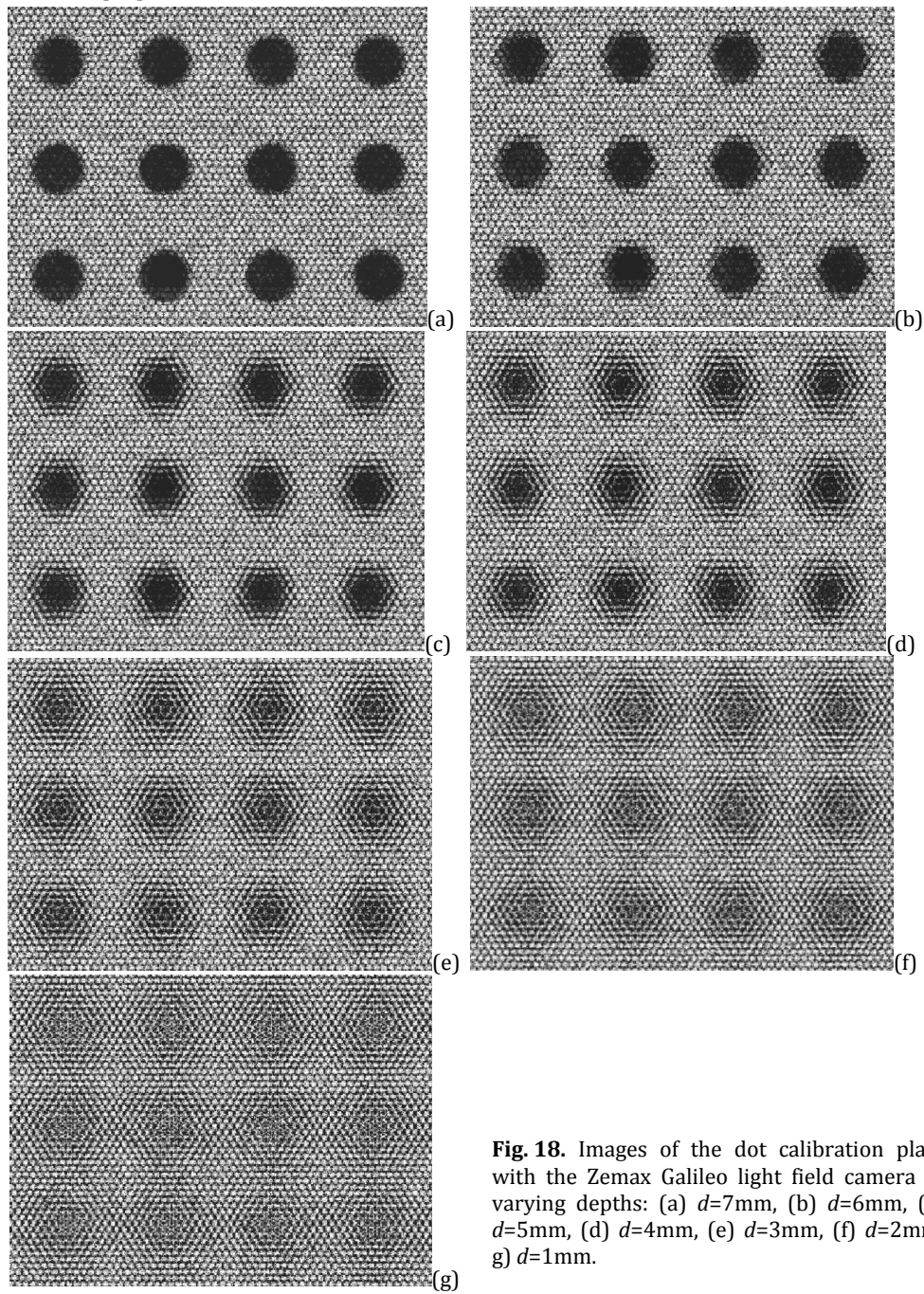
Fig. 18. Images of the dot calibration plate with the Zemax Galileo light field camera at varying depths: (a) d=7mm, (b) d=6mm, (c) d=5mm, (d) d=4mm, (e) d=3mm, (f) d=2mm, g) d=1mm.

After exporting the image of the dot calibration plate of the Zemax simulation system at the clearest imaging position, the previously established algorithm calculated the center of each microlens. Fig. 19 shows the calculation result, where the center points marked with red "+" symbols represent the calibrated centers of the microlenses. The results demonstrate a high level of accuracy in the calculations.


Fig. 19. The results of calculating the microlens center in the Zemax light field simulation system.

The next step is refocusing all the circular point calibration plate images obtained from different imaging positions within the simulation system for $\alpha \in (0.1 \sim 3.1)$, and calculating the $\alpha \sim \delta$ (δ represents the standard deviation of each pixel's grayscale value from the average grayscale value of the entire image, and it is used here to characterize the clarity of the image) curves and $d \sim \alpha_0$ calibration curves for different imaging positions. Figs. 20 and 21 show the results. Fig. 21 shows the depth calibration curve obtained. Based on this curve, the relationship between d and α_0 within the effective imaging range of the system designed can be known. When measuring, one can calculate the full focus map of the measured trajectory and then calculate the α_0 value of each pixel in the full focus map to obtain the corresponding d value (i.e., the value in the depth direction). Combined with the known two-dimensional information, the three-dimensional information of the entire trajectory in space can be obtained.

The simulated Galileo light field imaging system demonstrates clear recognition between d=7 mm and d=3 mm, while positions closer than 3 mm fall beyond the measurement range of the virtual light field system. When calibrating the depth, portions outside the measurement range are excluded.

During the design process, balancing spatial sampling and angular sampling is crucial. These factors exhibit a trade-off relationship in the second-generation light field imaging system. In the sampling process of a light field camera, the number of microlens arrays determines the spatial sampling of the system, and the number of pixels covered by a single microlens determines the angle sampling of the light field camera. The second-generation light field camera's sampling method differs from the first-generation light field camera, exchanging redundant angle resolution for more spatial resolution. Therefore, in the design of a microlens array, a balance must be struck between the size of a single microlens and the total number of microlenses [27].
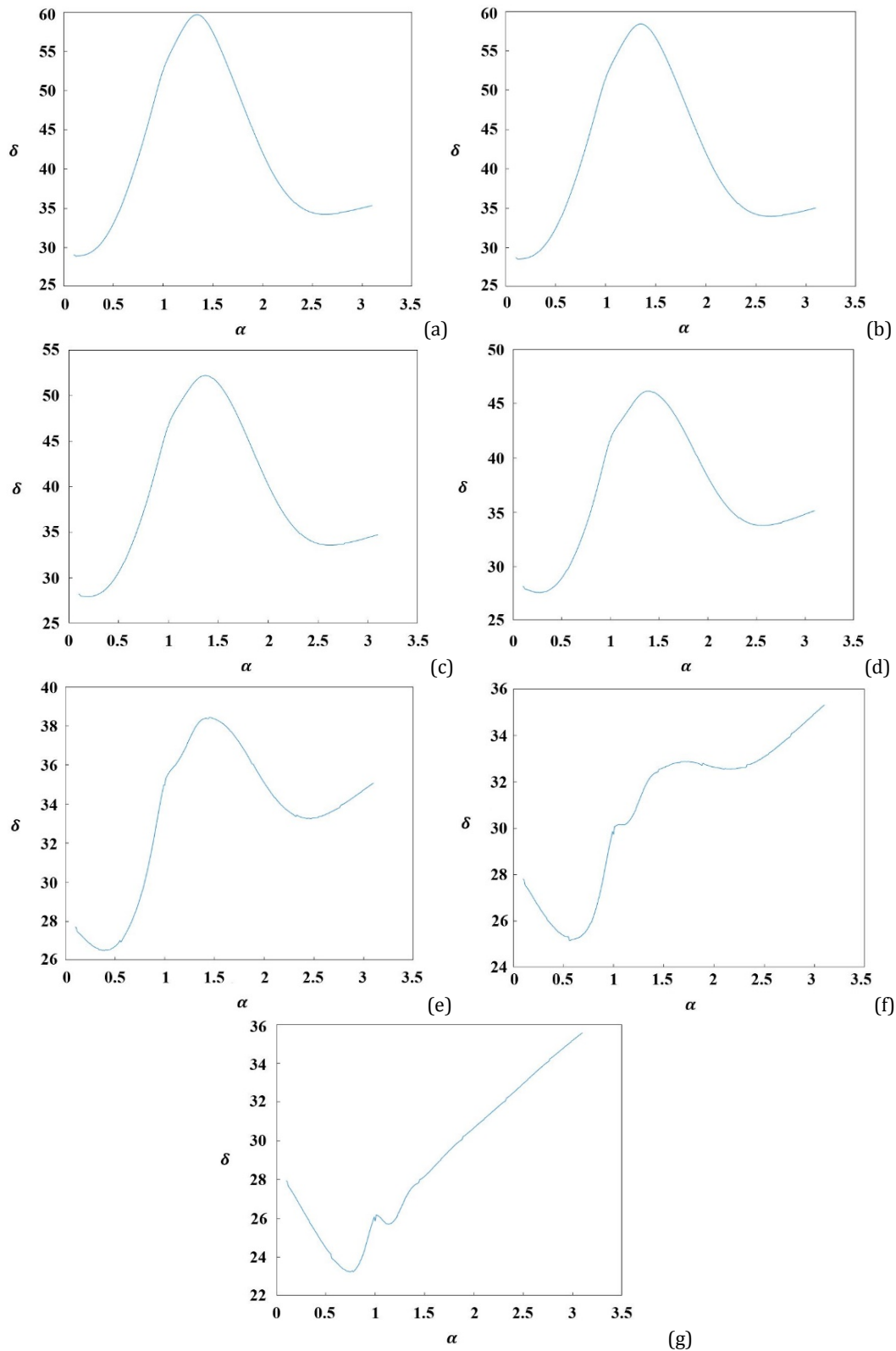
Fig. 20. Curves of $\alpha \sim \delta$ for the circular calibration plate at different positions in the improved Zemax light field system: (a) d=7mm, (b) d=6mm, (c) d=5mm, (d) d=4mm, (e) d=3mm, (f) d=2mm, (g) d=1mm.
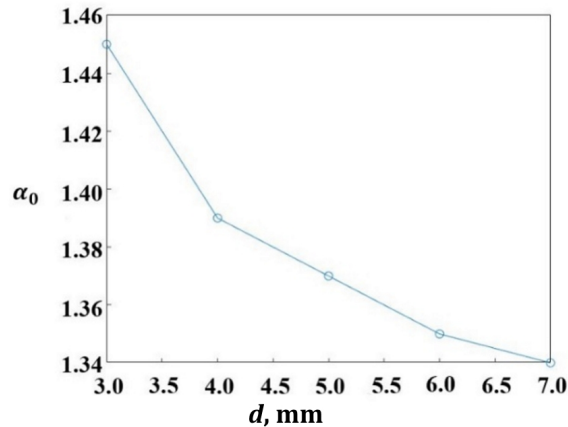
Fig. 21. Calibration curve of the improved Zemax light field simulation system $d \sim \alpha_0$.

5. Research of the PSV based on the simulated light field three-dimensional measurement system

Due to the limitations of Zemax simulation software in imaging dynamics, the algorithm requires multiple static images at different time points and depth positions to synthesize virtual light field trajectory maps.

In this study, a square black pixel block is used as the original experimental image and imported into the virtual light field imaging system for analysis.

After importing the original black square pixel block image into the virtual light field imaging system, with a working distance of 7 mm, the light field image is exported. Subsequently, the black pixel block is moved 6 pixels to the right, imported into the Zemax light field simulation system, and imaged with the working distance set to 6.9 mm. This process repeats, reducing the working distance by 0.1 mm for every 6-pixel movement of the black pixel block towards the right until the working distance reaches 3 mm.

The process involved 41 black pixel blocks at different positions and working distances. Fig. 22 presents the light field simulation imaging results at various positions and working distances of the black square pixel blocks.

The algorithm retrieved a light field trajectory map with an imaging depth ranging from 7 mm to 3 mm by combining and processing all the light field images at different positions and working distances. Fig. 23 shows the resulting simulation trajectory diagram for the Zemax light field system.

According to the optical field PSV three-dimensional measurement algorithm established in reference [21], the virtual optical field trajectory map undergoes refocusing and focusing processing. The resulting full-focus map is color-reversed and then processed sequentially through binarization, erosion and expansion, removal of small targets, skeleton extraction, and elimination of intersection lines. Finally, the two-dimensional position map of the trajectory is obtained, as shown in Fig. 24.

By combining the obtained depth calibration curve of the virtual light field system $d \sim \alpha_0$ as shown in Fig. 23, the three-dimensional information of the virtual light field trajectory map was derived, as shown in Fig. 25.
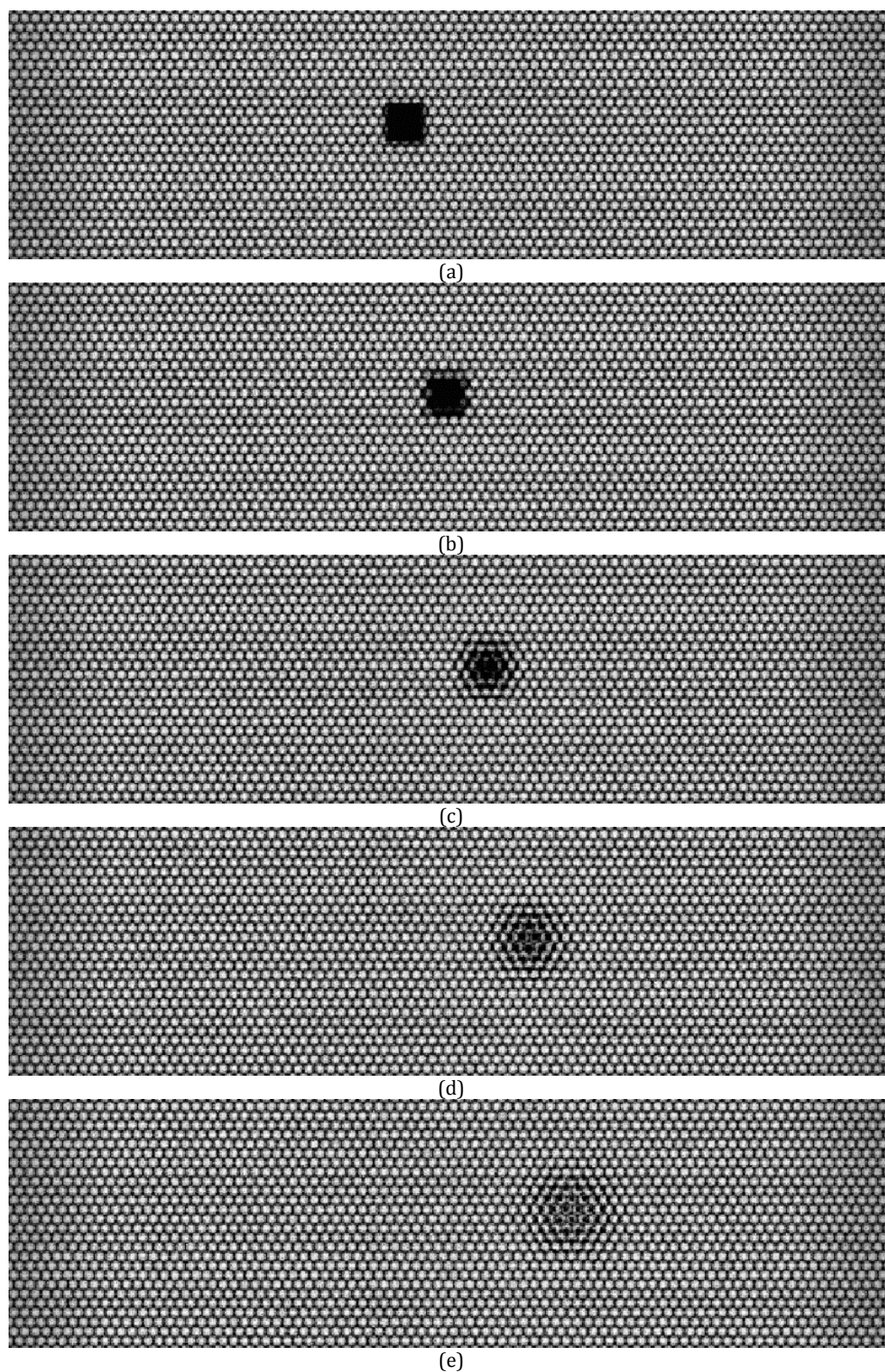
Fig. 22. Simulated light field imaging results of the black square at different positions and imaging distances: (a) d=7 mm, (b) d=6 mm, (c) d=5 mm, (d) d=4 mm, (e) d=3 mm.
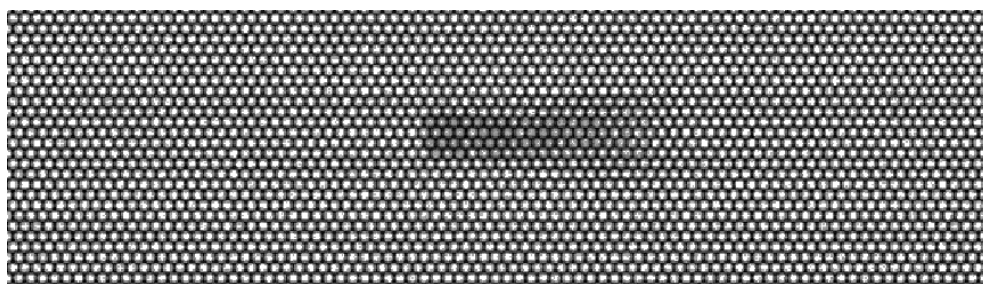
Fig. 23. Simulated trajectory diagram of the Zemax light field system.
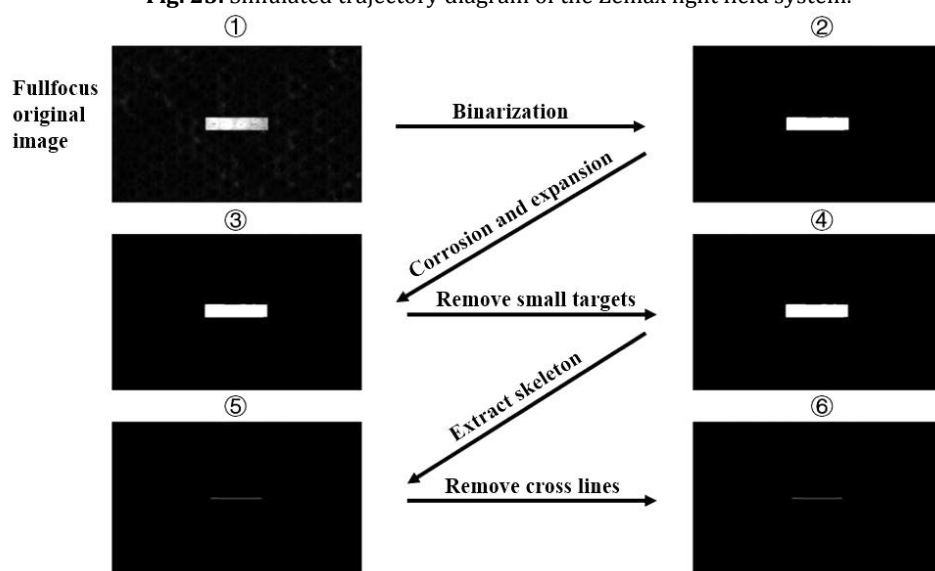

Fig. 24. Two-dimensional preprocessing diagram of the Zemax light field system simulation trajectory.
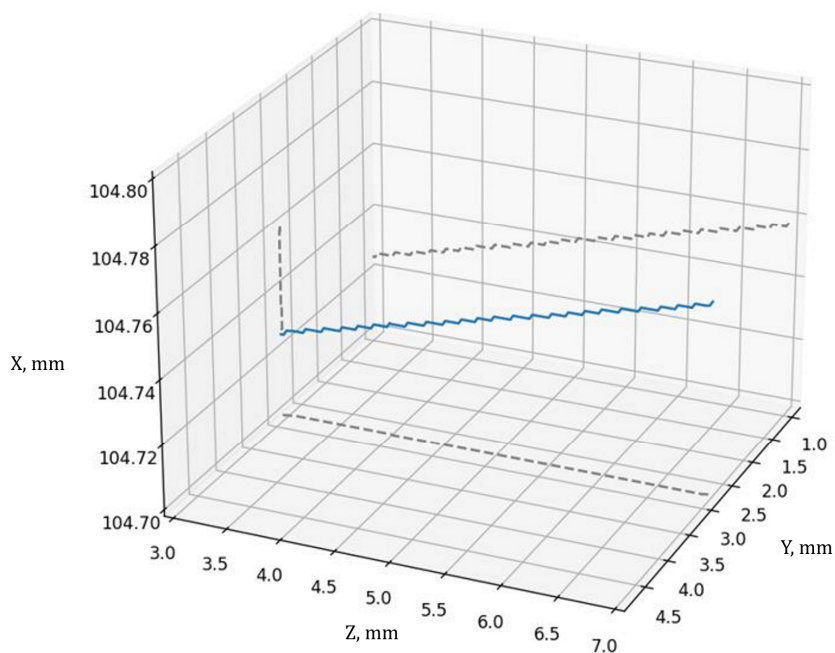

Fig. 25. Three-dimensional imaging of the simulated trajectory of the Zemax light field system. The dashed lines indicate the projections of the trajectory into the coordinate planes.

6. Conclusions and outlook

This article uses Zemax software to construct a simulated virtual Galileo-type light field camera, analyze the imaging characteristics of the simulated light field system, and derive the depth calibration curve of the Zemax-simulated virtual light field imaging system. Additionally, a virtual light field three-dimensional trajectory map was synthesized and combined with the depth calibration curve of the simulated light field imaging system and the established light field PSV three-dimensional flow field processing algorithm. This method allowed for the extraction of three-dimensional information from the virtual motion trajectory, establishing a simulated light field PSV three-dimensional measurement system.

However, the PSV 3D flow field processing algorithm based on light field imaging presented in this article cannot currently determine the direction of the trajectory. In experimental applications, it must be inferred indirectly by manipulating exposure times to produce distinct trajectory patterns, such as "short-long-short" or "long-long-short" configurations.

Future advancements in this domain will require collaborative efforts from scholars to develop a robust 3D flow field measurement algorithm based on light field PSV, capable of accurately determining trajectory direction. Such innovations would significantly enhance the utility and precision of light field imaging in three-dimensional flow field measurement.

References

1. Gershun, A. (1939). The light field. Journal of Mathematics and Physics, 18(1-4), 51-151.
2. McMillan, L., & Bishop, G. (2023). Plenoptic modeling: An image-based rendering system. In Seminal Graphics Papers: Pushing the Boundaries, Volume 2 (pp. 433-440).
3. Levoy, M., & Hanrahan, P. (2023). Light field rendering. In Seminal Graphics Papers: Pushing the Boundaries, Volume 2 (pp. 441-452).
4. Yang, J. C., Everett, M., Buehler, C., & McMillan, L. (2002). A real-time distributed light field camera. Rendering Techniques, 2002(77-86), 2.
5. Wilburn, B., Joshi, N., Vaish, V., Talvala, E. V., Antunez, E., Barth, A., Adams, A., Horowitz, M. & Levoy, M. (2005). High performance imaging using large camera arrays. In ACM siggraph 2005 papers (pp. 765-776).
6. 6. Ng, R., Levoy, M., Brédif, M., Duval, G., Horowitz, M., & Hanrahan, P. (2005). Light field photography with a hand-held plenoptic camera (Doctoral dissertation, Stanford university).
7. Lanman, D., Crispell, D., Wachs, M., & Taubin, G. (2006, June). Spherical catadioptric arrays: Construction, multi-view geometry, and calibration. In Third International Symposium on 3D Data Processing, Visualization, and Transmission (3DPVT'06) (pp. 81-88). IEEE.
8. Veeraraghavan, A., Raskar, R., Agrawal, A., Mohan, A., & Tumblin, J. (2007). Dappled photography: Mask enhanced cameras for heterodyned light fields and coded aperture refocusing. ACM Trans. Graph., 26(3), 69.
9. 9. Taguchi, Y., Agrawal, A., Ramalingam, S., & Veeraraghavan, A. (2010, June). Axial light field for curved mirrors: Reflect your perspective, widen your view. In 2010 IEEE Computer Society Conference on Computer Vision and Pattern Recognition (pp. 499-506). IEEE.
10. Venkataraman, K., Lelescu, D., Duparré, J., McMahon, A., Molina, G., Chatterjee, P., Mullis, R, & Nayar, S. (2013). Picam: An ultra-thin high performance monolithic camera array. ACM Transactions on Graphics (TOG), 32(6), 1-13.
11. Kim, C., Zimmer, H., Pritch, Y., Sorkine-Hornung, A., & Gross, M. H. (2013). Scene reconstruction from high spatio-angular resolution light fields. ACM Trans. Graph., 32(4), 73-1.
12. Marwah, K., Wetzstein, G., Bando, Y., & Raskar, R. (2013). Compressive light field photography using overcomplete dictionaries and optimized projections. ACM Transactions on Graphics (TOG), 32(4), 1-12.
13. Lin, X., Wu, J., Zheng, G., & Dai, Q. (2015). Camera array based light field microscopy. Biomedical Optics Express, 6(9), 3179-3189.
14. Antipa, N., Necula, S., Ng, R., & Waller, L. (2016, May). Single-shot diffuser-encoded light field imaging. In 2016 IEEE International Conference on Computational Photography (ICCP) (pp. 1-11). IEEE.

15. Tan, Z. P., Johnson, K., Clifford, C., & Thurow, B. S. (2019). Development of a modular, high-speed plenoptic-camera for 3D flow-measurement. Optics Express, 27(9), 13400-13415.

16. Zhu, X., Zhang, B., Li, J., & Xu, C. (2020). Volumetric resolution of light field imaging and its effect on the reconstruction of light field PIV. Optics Communications, 462, 125263.

17. Kvon, A. Z., Bobylev, A. V., Guzanov, V. V., & Kharlamov, S. M. (2020, November). Application of the PTV with the use of a light-field camera to study three-dimensional wave regimes of liquid film flow. In Journal of Physics: Conference Series (Vol. 1677, No. 1, p. 012069). IOP Publishing.

18. Zhang, D., Tropea, C., Zhou, W., Cai, T., Huang, H., Dong, X., Gao, L & Cai, X. (2024). Particle streak velocimetry: a review. Experiments in Fluids, 65(9), 130.

19. Dong, X., Wang, X., Zhou, W., Wang, F., Tang, X., & Cai, X. (2023). 3D particle streak velocimetry by defocused imaging. Particuology, 72, 1-9.

20. Sold, S., Rädle, M., & Repke, J. U. (2025). Extended particle streak velocimetry (E-PSV) for a comprehensive view of film flows. Experiments in Fluids, 66(1), 19.

21. Yang, M. (2024). A Three-Dimensional Flow Field Measurement Method Based on Light Field Particle Streak Velocimetry. Ukrainian Journal of Physical Optics, 25(4), 04038-04050.

22. Adelson, E. H., & Bergen, J. R. (1991). The plenoptic function and the elements of early vision (Vol. 2). Cambridge, MA, USA: Vision and Modeling Group, Media Laboratory, Massachusetts Institute of Technology.

23. Lynch, K. (2011). Development of a 3-D fluid velocimetry technique based on light field imaging. Auburn University.

24. Georgiev, T., & Intwala, C. (2006). Light field camera design for integral view photography. Adobe System, Inc., Technical Report, 1.

25. Ahrenberg, L., & Magnor, M. (2006). Light field rendering using matrix optics. WSCG2006 Full Papers Proceedings, 177-184.

26. Cao, L., Zhang, B., Li, J., Song, X., Tang, Z., & Xu, C. (2019). Characteristics of tomographic reconstruction of light-field Tomo-PIV. Optics Communications, 442, 132-147.

27. Georgiev, T., & Lumsdaine, A. (2010). Focused plenoptic camera and rendering. Journal of Electronic Imaging, 19(2), 021106-021106.

Анотація. Технологія візуалізації світлового поля може фіксувати інтенсивність світла та напрямок його поширення в межах однієї експозиції, що дозволяє виконувати тривимірну візуалізацію, спрощуючи при цьому складність експерименту. У порівнянні з традиційними методами, такими як анемометрія за зображеннями частинок і анемометрія за відстеженням частинок, анемометрія за треками частинок (PSV) розширює верхню межу вимірюваної швидкості, ефективно працює при меншій інтенсивності світла та має суттєві переваги при аналізі високошвидкісних потоків. Інтеграція методів візуалізації світлового поля та вимірювання PSV поєднує в собі сильні сторони обох методів, що робить цей підхід особливо перспективним для тривимірних досліджень поля потоку. Попри великий потенціал, ця галузь залишається недостатньо вивченою. Раніше автором була розроблена тривимірна система експериментального вимірювання поля потоку на основі світлового поля PSV. У цій статті автор використовує програмне забезпечення Zemax для створення системи моделювання зображення світлового поля Галілеєвого типу в непослідовному режимі. Були проаналізовані характеристики зображення цієї системи, що дозволило отримати калібрувальну криву глибини для змодельованої віртуальної системи візуалізації світлового поля та синтетичну тривимірну карту траєкторії. Тривимірна траєкторія була реконструйована за допомогою цього алгоритму шляхом інтеграції кривої калібрування глибини з алгоритмом вимірювання та обробки тривимірного поля потоку на основі світлового поля PSV. Цим дослідженням встановлено структуру моделювання Zemax для світлового поля PSV і запропоновано важливі дані моделювання для досліджень тривимірного вимірюванні поля потоку з використанням світлового поля PSV.

Ключові слова: візуалізація світлового поля, велосиметрія за треками частинок, 3D вимірювання, моделювання Zemax